Article

Synthesis, Molecular Structure, Thermal and Spectroscopic Analysis of a Novel Bromochalcone Derivative with Larvicidal Activity

Pollyana P. Firmino [1,2], Jaqueline E. Queiroz [3], Lucas D. Dias [2], Patricia R. S. Wenceslau [1], Larissa M. de Souza [2], Ievgeniia Iermak [2], Wesley F. Vaz [1], Jean M. F. Custódio [4], Allen G. Oliver [4], Gilberto L. B. de Aquino [1,3] and Hamilton B. Napolitano [1,*]

1   Grupo de Química Teórica e Estrutural de Anápolis, Universidade Estadual de Goiás, Anápolis 75132-903, GO, Brazil; polly.firmino@outlook.com (P.P.F.); patricia.wenceslaubio@gmail.com (P.R.S.W.); wesfonseca@gmail.com (W.F.V.); gilbaqui@hotmail.com (G.L.B.d.A.)
2   São Carlos Institute of Physics, University of São Paulo, São Carlos 13566-590, SP, Brazil; lucasdanillodias@gmail.com (L.D.D.); larissamarila@hotmail.com (L.M.d.S.); ievgeniia.iermak@gmail.com (I.I.)
3   Laboratório de Pesquisa em Bioprodutos e Síntese, Universidade Estadual de Goiás, Anápolis 75132-903, GO, Brazil; jaqueevan.je@gmail.com
4   Department of Chemistry and Biochemistry, University of Notre Dame, Notre Dame, IN 46556, USA; jeanmfcustodio@gmail.com (J.M.F.C.); aoliver2@nd.edu (A.G.O.)
*   Correspondence: hamilton@ueg.br

Abstract: Chalcones belong to the flavonoids family and are natural compounds which show promising larvicidal property against *Aedes aegypti* larvae. Aiming to obtain a synthetic chalcone derivative with high larvicidal activity, herein, a bromochalcone derivative, namely (*E*)-3-(4-butylphenyl)-1-(4-bromophenyl)-prop-2-en-1-one (BBP), was designed, synthesized and extensively characterized by [1]H- and [13]C- nuclear magnetic resonance (NMR), infrared (IR), Raman spectroscopy, mass spectrometry (MS), ultraviolet–visible spectroscopy (UV-Vis), thermogravimetric analysis (TGA), differential scanning calorimetry (DSC), and X-ray diffraction. Further, the quantum mechanics calculations implemented at the B3LYP/6–311+G(d)* level of the theory indicate that the supramolecular arrangement was stabilized by C–H⋯O and edge-to-face C–H⋯π interactions. The EGAP calculated (3.97 eV) indicates a good reactivity value compared with other similar chalcone derivatives. Furthermore, the synthesized bromochalcone derivative shows promising larvicidal activity (mortality up to 80% at 57.6 mg·L^{-1}) against *Ae. aegypti* larvae.

Keywords: bromochalcone; X-ray diffraction; B3LYP/6-311+G(d); larvicide; *A. aegypti* larvae

1. Introduction

Chalcones are open-chain flavonoid compounds with an α,β-unsaturated, carbonyl group consisting of two aromatic rings with a range of substituents [1,2]. These molecules can be isolated from pigments commonly found in plants or synthesized by the classic Claisen–Schmidt method [3–5]. This class is a privileged structure with biological activities such as anti-inflammatory [6], anticancer [7,8], antifungal [9,10], antibacterial [2], antioxidant [11], and antiparasitary [12,13]. Likewise, substituting groups on the aromatic rings of chalcone can modulate its larvicidal activity. In this context, the understanding of the structure–activity relationship of chalcones and their larvicidal activity is still a challenge.

Yellow fever, chikungunya, dengue fever, and Zika are infectious diseases transmitted by the bite of the *Aedes aegypti* mosquito [14]. It is calculated that more than 2.5 billion people live in transmission risk areas (e.g., Brazil, some African countries) [15]. Due to the absence of a prophylactic vaccine, these infectious diseases can only be contained by combating the

vector insect [16]. Nowadays, one of the most accepted methods for controlling infectious diseases transmitted by *Ae. aegypti* is through the application of chemical larvicides. Organophosphate, organochlorine, and synthetic pyrethroid insecticides are used in public health control measures [17]. Nevertheless, these larvicides still show some issues e.g., (i) low selectivity, (ii) environment damage, and (iii) toxicity for humans. In this regard, chalcones (a natural product) have been tested as a potential larvicide, showing promising results [18–21].

To obtain a chalcone derivative with larvicidal activity, herein, we reported the design, synthesis, and structural description of a chalcone, namely (*E*)-3-(4-butylphenyl)-1-(4-bromophenyl)-prop-2-en-1-one (BBP) (Figure 1), using the density functional theory (DFT) implemented at the B3LYP/6–311+G(d)* level of the theory [22–24]. Moreover, this work describes the full characterization of BBP by nuclear magnetic resonance (NMR), infrared (IR), Raman spectroscopy, mass spectrometry (MS), ultraviolet–visible spectroscopy (UV-Vis), thermogravimetric analysis (TG), and differential scanning calorimetry (DSC). Additionally, the supramolecular arrangements were analyzed by X-ray diffraction and Hirshfeld surfaces (HS) to understand the electrophilic and nucleophilic reactions, and hydrogen bond interactions' connectivity [22,25] was observed, which may influence its larvicidal activity. Furthermore, the larvicidal activity (mortality) of BBP against *Ae. aegypti* larvae (L3) were evaluated.
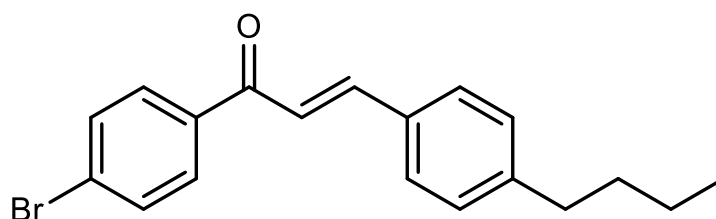

Figure 1. Molecular structure of 3-(4-butylphenyl)-1-(4-bromophenyl)-prop-2-en-1-one (BBP).

2. Materials and Methods

2.1. Synthesis and Crystallization

Chemicals and solvents required for BBP synthesis were obtained from commercial sources and used without further purification. 4-Butylbenzaldehyde (1 mmol; 162.3 mg) and 4′-bromo-acetophenone (1 mmol; 199.0 mg) were added in ethanol (0.5 mL). Then, pulverized KOH (1 mmol; 56.1 mg) was added, and the reaction mixture was kept under manual shaking for 3 min at 25 °C. The reaction's progress was monitored by thin-layer chromatography (TLC) (silica gel 60 UV254 plate), using CH_2Cl_2 as an eluent. Then, crystals were obtained and collected by vacuum filtration, followed by a crystallization process using ethanol as a solvent. BBP was obtained in 95% yield (0.95 mmol; 326.0 mg). $C_{19}H_{19}BrO$ (342.06 g/mol); white solid, and m.p. 109.8 °C. To grow BBP crystals, the finely powdered sample was added to a conical flask with a known volume of dichloromethane, then the solution was recrystallized by the diffusion of pentane vapor in a dichloromethane solution and kept at room temperature for slow evaporation for 72 h until crystal formation.

2.2. Spectroscopic and Thermal Characterization

A Bruker Avance 500MHZ NMR spectrometer was used to obtain ^{1}H- and ^{13}C-NMR spectra using TMS as the internal standard and $CDCl_3$ as the solvent. The corresponding shifts reveal the purity of the compound.

The IR spectrum was recorded using a Perkin Elmer (8400S FT-IR) spectrometer in the wavenumber range 400–4000 cm^{-1} by the KBr technique. Raman measurements were performed on a WITec Alpha 300 RAS microscope (WITec, Ulm, Germany). The excitation wavelength was 785 nm, the detection range was 100–4000 cm^{-1}, with the resolution of 1 cm^{-1}. The spectra were collected with a 20× magnification objective (Zeiss, Jena, Germany). Spectra were recorded with the integration time of 30 s and 2 accumulations. Obtained spectra were processed using WITec Project FOUR and Origin 2016 software.

Gas chromatogram and mass spectrum (GC-MS) were recorded in Shimadzu (QP2010 Ultra) equipped with capillary column CBP-5 (30 × 0.25 × 0.25); the injection volume was 1.0 μL in split mode and helium as drag gas with 1.0 mL.min-1 flow. The injector temperature was 280 °C, and the detector was 310 °C. The initial oven temperature was 100 °C (for 2 min), followed by a heating ramp of 30 °C.min^{-1} till 300 °C, then 300 °C for 10 min. Solid-state UV-vis spectra were obtained using a Cary 5000 UV-Vis-NIR spectrometer. IR (KBr): 1659 υ(C=O); 1599 υ(C=C); 1419 υ(C=C) aromatic ring; 987 υ(CH=CH); 571 υ(C-Br) cm^{-1}; FT-Raman: 1659 υ(C=O); 1599 υ(C=C); 1421 υ(C=C) aromatic ring; 989 υ(CH=CH); 699 υ(C–Br) cm^{-1}; MS (m/z): 342, 344, 287, 285, 263 and 57; UV-vis (DMSO): λ = 213, 336 nm.

TGA was performed in the Perkin Elmer Pyris (1TGA model) equipment. The evaluation was carried out with a 2.131 mg sample mass in an alumina crucible. The TGA was performed on the BBP compound at an initial temperature ranging from 25 °C to 600 °C, with a heating rate of 10 °C·min^{-1} under nitrogen purge gases with 20 mL·min^{-1} flow. DSC (214 Polyma, Netzsch) measurements were carried out in platinum crucibles with the crucibles sealed without drilling the lid. A sample weighing 1.91 mg was used in the crucibles. The temperature range was 20–200 °C applied at a heating rate of 10 °C·min^{-1}, under a dynamic 5.0 N_2 atmosphere of 40 mL·min^{-1}. For these analyses, a correction was performed to eliminate the background.

2.3. X-ray Diffraction Analysis

A suitable crystal of BPP was selected, kept at 119.99 K, and the X-ray diffraction was collected on a Bruker APEX-II CCD diffractometer with wavelength radiation MoKα λ = 0.71073 Å. The size of the crystal used was 0.226 × 0.197 × 0.044 mm^3. The structure was solved by direct methods with the intrinsic phasing method (SHELXT) [26] using Olex2 1.3 version [27] and refined by least-squares minimization with SHELXL [28]. All hydrogen atoms were fixed at the calculated position, and potential hydrogen–bond interactions were verified through Platon [29]. The structure data were deposited in the Cambridge Crystallography Data Center (CCDC) under code 2069836.

The HS was generated using a standard (high) surface resolution with the three-dimensional dnorm surfaces mapped over a red to blue [30] fixed-color scale, which is shorter than the white surface that indicates contacts with distances equal to the sum of van der Waals [31]. HS is a tool to assess observed intermolecular interactions and is defined by the weight function w(r) [32]. It is calculated for each atom in a crystal by Equation (1) and can be determined using Crystal Explorer software [33,34].

$$w(r) = \frac{\sum_{molecule} \rho_i^{at}(r)}{\sum_{crystal} \rho_i^{at}(r)} \tag{1}$$

The ρ(r) is the average density, the numerator is a sum over the atoms in the molecule, and the denominator is the sum over the crystal [33].

2.4. Theoretical Analysis

Electronic calculations were undertaken from experimentally determined atom coordinates. The geometry optimization and vibrational modes were carried out using the Gaussian 09 [35] packages, through DFT applying B3LYP/6-311+G(d)* as the functional and basis set to confirm the stability associated with optimized geometries of molecules [36–38], and a scale factor of 0.9686 was used to mitigate the effects of overestimation in the vibration values calculated via DFT, obtaining better convergence with the experimental values [39–42]. To check that the optimized geometry was found in a local minimum, analytic harmonic frequency calculations were undertaken at the identical level of theory. The absence of imaginary frequencies reveals that the optimized structure is truly at a local minimum. The highest occupied molecular orbital (HOMO), the lowest unoccupied molecular orbital (LUMO), and the molecular electrostatic potential (MEP) map were graphically represented by Gaussview 6.0 software (Wallingford, Connecticute, USA) [43].

2.5. Larvicidal Assays

Aedes aegypti (Rockefeller strain) eggs were provided by Prof. Alex Martins Machado from the Laboratory of Virology and Cell Culture at the Federal University of Mato Grosso do Sul, MS, Brazil. These eggs were hatched in a plastic tray containing 1.5 L of dechlorinated water and kept in an incubator under controlled conditions (at 27 ± 2 °C under 12:12 h light/dark photoperiod with $73.0 \pm 0.4\%$ relative humidity). Once a day, the larvae were fed with a blend of powdered fish food AlconBASIC® MEP 200 Complex (Alcon, Camboriú, SC, Brazil) and dry yeast, in a 3:1 proportion. Larvae were collected at the third stage (L3) to be used in the larvicidal assays.

Larvicidal activity assays were performed according to Targanski et al. (2021) [18]. Each bioassay consisted of incubating 10 larvae (L3) in distilled water (20 mL), containing different concentrations of chalcone (7.2–57.6 mg·L^{-1}). An equivalent volume to the highest concentration tested (57.6 mg·L^{-1}) was used as a negative control. Larval mortality (%) was recorded after 48 h. All experiments were carried out in triplicate. The LC25, LC50, and LC75 values of *Ae. aegypti* larvae were estimated by non-linear regression, calculated using Origin 2020 software (OriginLab Corp. 9.7).

3. Results

3.1. Synthesis and Crystallization

BBP chalcone was synthesized by the Claisen–Schmidt condensation protocol. In this procedure, 4-butylbenzaldehyde, 4′-bromo-acetophenone, and KOH were added in ethanol and were reacted by manual shaking for 3 min, at 25 °C (Scheme 1). BBP was obtained in 95% yield (0.95 mmol; 326.0 mg). High-quality crystals of BBP were obtained, and the molecular modeling analysis was performed.
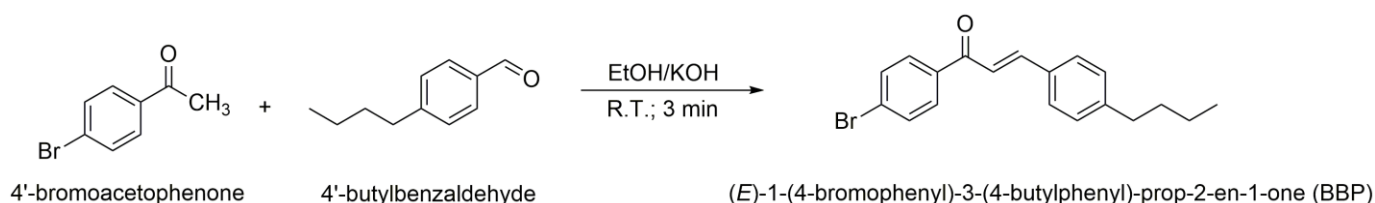
Scheme 1. Synthesis of 3-(4-butylphenyl)-1-(4-bromophenyl)-prop-2-en-1-one (BBP).

3.2. Structural Analysis

The BBP compound was characterized by IR, Raman, ^{1}H- and ^{13}C NMR, MS, TGA, DSC, UV-Vis, and X-ray diffraction. The characteristic peaks were observed in the FT-infrared spectroscopy (IR) overlaying the FT-theoretical vibrational frequencies Figure 2. FT-Raman Figure 3 was carried out on the prior fully optimized geometry at B3LYP/6-311+G(d). The frequencies are presented in Table 1 and are consistent with the functional groups present in the BBP. Moreover, Figures 4 and 5 show ^{1}H- and ^{13}C-NMR spectra of BBP, respectively. These spectra were used to identify the sample purity and structural conformation of BBP. From the analysis of the spectra, the following chemical shifts are present: ^{1}H-NMR (500 MHz, CDCl$_3$) δ 7.87 (d, *J* = 8.6 Hz, 1H), 7.79 (d, *J* = 15.7 Hz, 1H), 7.63 (d, *J* = 8.6 Hz, 1H), 7.55 (d, *J* = 8.1 Hz, 1H), 7.42 (d, *J* = 15.6 Hz, 1H), 7.23 (d, *J* = 8.1 Hz, 1H), 2.65 (d, *J* = 7.7 Hz, 1H), 1.62 (dq, *J* = 12.9, 7.6 Hz, 1H), 1.43–1.31 (m, 1H), 0.93 (t, *J* = 7.4 Hz, 2H); ^{13}C-NMR (126 MHz, CDCl$_3$): δ 195.37, 144.42, 136.81, 133.86, 133.52, 132.27, 132.24, 131.88, 130.46, 129.86, 128.52, 127.60, 127.49, 127.30, 126.58, 125.60, 125.04, 124.53.

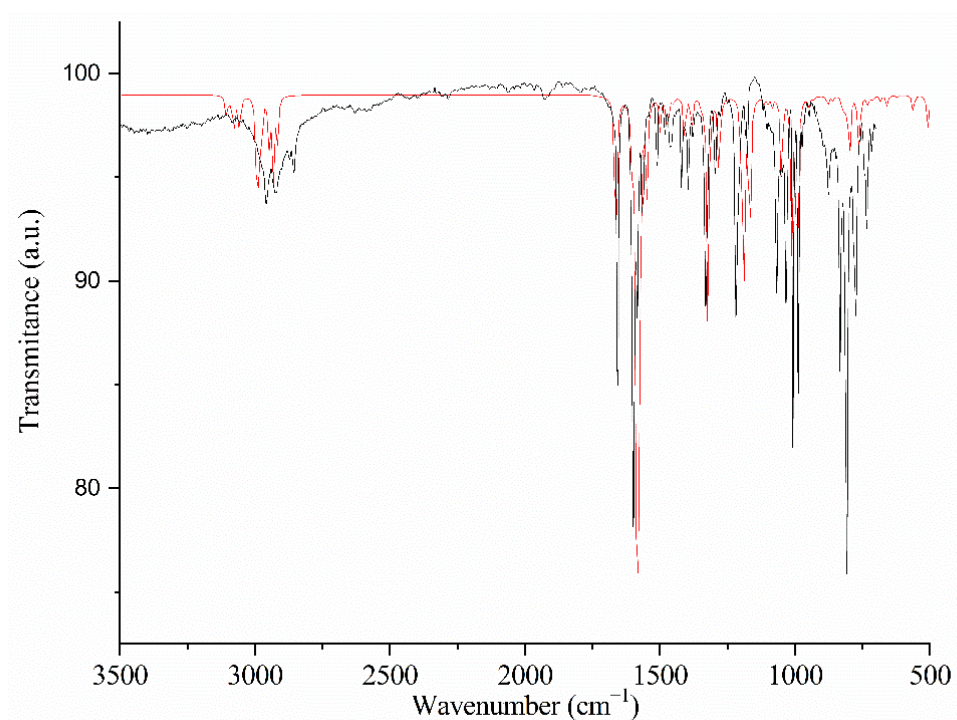**Figure 2.** IR Overlay for FT-infrared spectrum of BBP in black and FT-theoretical vibrational frequencies in red.
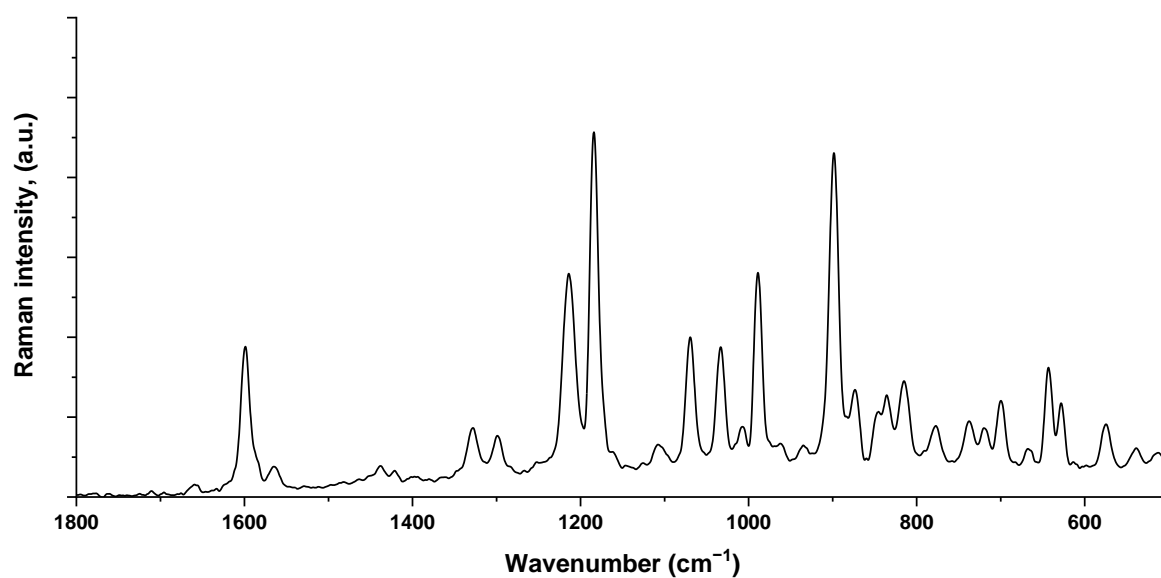

Figure 3. FT-Raman spectrum of BBP.

Table 1. Assignments of FT-IR; theoretical FT-IR and FT-Raman spectral bands for BBP.

Infrared Bands (cm^{-1})	Theoretical Infrared Bands (cm^{-1})	Raman Bands (cm^{-1})	Assignment
2953	3051.14–3107.11	2993	υ(C–H) aromatic
2924	2914.51–2992.48	–	υ(C–H)
2853	3051.14	–	υ(=C–H)
1659	1662.49	1661	υ(C=O)
1599	1582.93	1599	υ(C=C)
1419	1547.44–1603.37	1421	υ(C=C) aromatic ring
1330	1302.72	1328	δ(–C–H)
–	–	1299	δ(C–H)
1219		1297, 1327, 1421, 1437	δ(C–C)
1185	1113.46–1172.86	1180	δ(C–H) aromatic in plane
1068	1039.37	1069	υ(C–C) alicyclic, aliphatic chain vibrations
987	990.73	989	υ(CH=CH)
832, 810, 773	816.92	898	δ(C=O) in plane
571	–	699	υ(C–Br)
-		703, 716, 738, 776, 813, 836, 871, 898, 990	δ(C–C) aliphatic chains

υ: stretching vibrations. δ: bending vibrations.
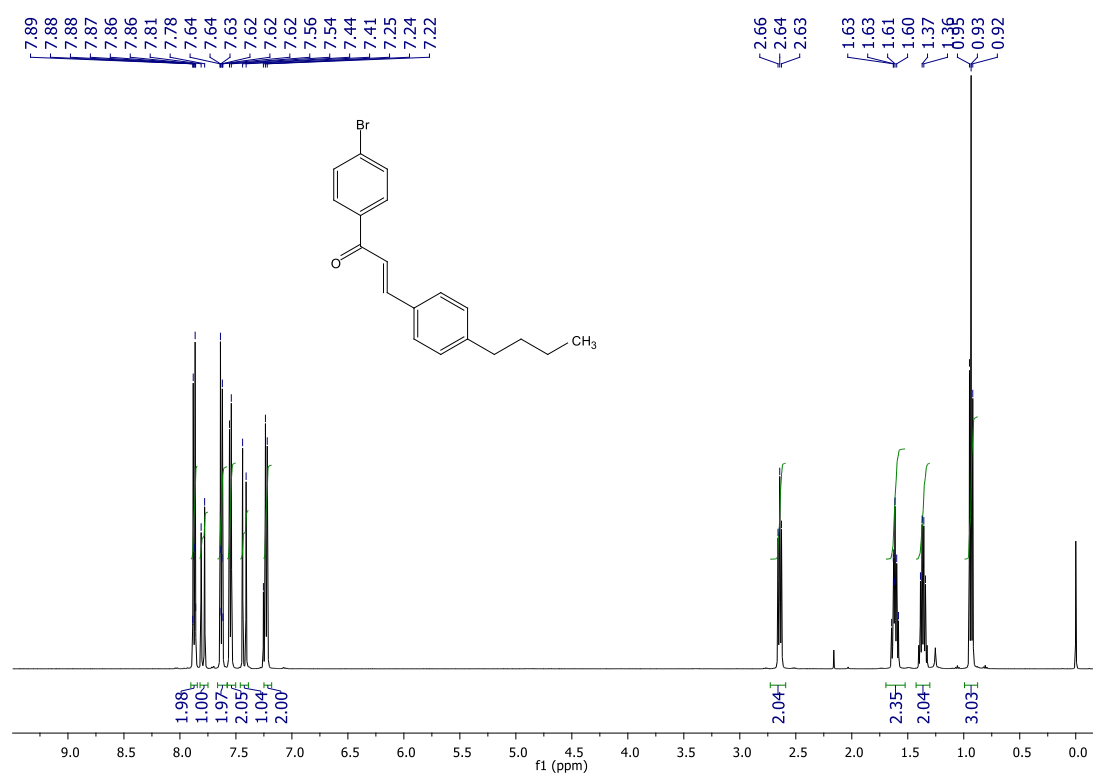
Figure 4. ^{1}H-NMR spectrum of BBP.

Figure 5. ^{13}C-NMR spectrum of BBP.
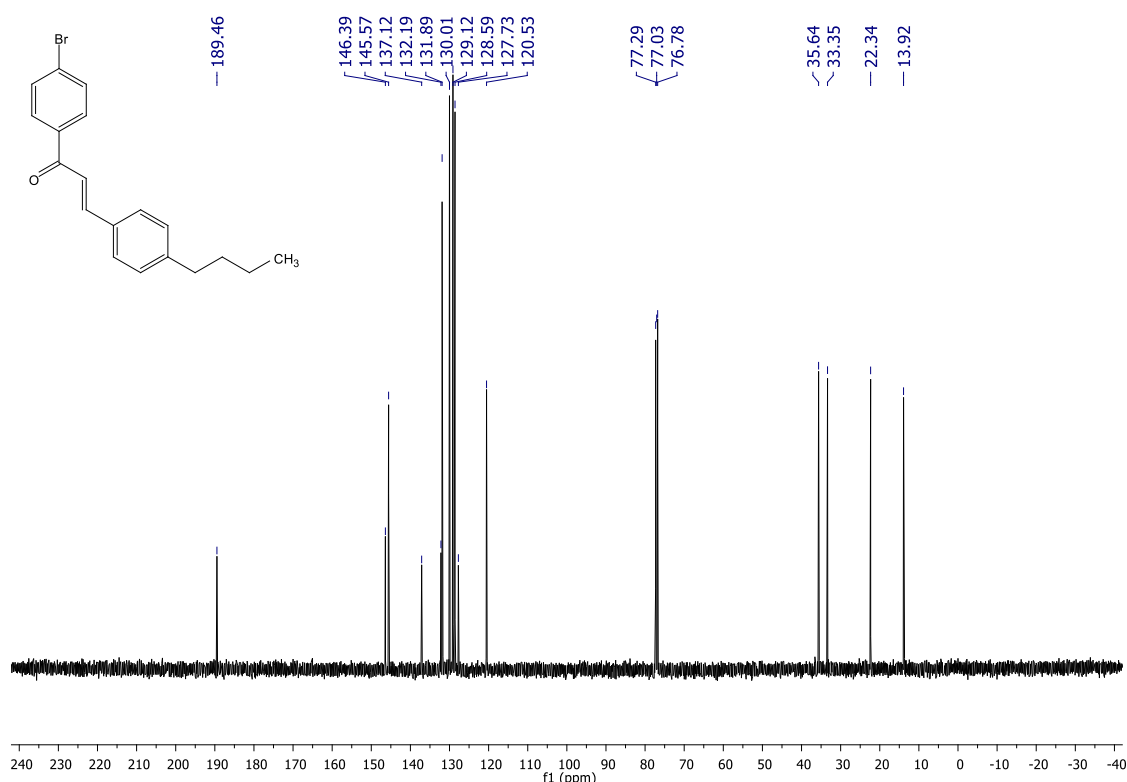
The results of the theoretical FT-IR show that the aromatic C−H stretching band occurs in the range of 3052–3107 cm^{-1}; experimentally, this vibration is observed at 2953 cm^{-1}. The C−H stretching vibrations emerge at the range of 2914–2992 cm^{-1}; experimentally, this vibration is observed at 2924 cm^{-1}. Regarding the C–H stretching vibrations in the vinyl group, these were observed at 3051 cm^{-1}, while experimentally they were observed at 2853 cm^{-e}. The theoretical bands observed at 1662 cm^{-1} are assigned to stretching of the C=O group, while the experimental band is observed at 1659 cm^{-1}. In terms of C=C stretching, this is assigned a calculated band at 1582 cm^{-1}; this value is closer to that obtained experimentally: 1599 cm^{-1}. Furthermore, the calculated –C–H bending vibration modes were found at 1302 cm^{-1}, while experimentally they arise at 1330 cm^{-1}. Moreover, for aromatic C–H in plane mode, the theoretical value is 1113–1172 cm^{-1}; experimentally, it occurs at 1185 cm-1. The alicyclic C–C and CH=CH theoretical stretching vibrations are observed at 1039 and 990 cm^{-1}, respectively. Meanwhile, experimental bands are assigned at 1068 and 987 cm^{-1}, respectively. Finally, the C=O in-plane bending vibrations arise at 816 cm^{-1}, while the experimental values are in the 832, 810, and 773 cm^{-1} regions. All these values are listed in Table 1.

The theoretical IR band data were supported by analyses from the animation option of Gaussview 6 [43]. The observed differences between the theoretical and the experimental findings could be explained by the fact that experiments were performed on a crystalline conformation of the sample, while the theoretical calculations were made for a free molecule, thus being systematically overestimated for vibrational frequencies [22]. Raman spectroscopy was also used to characterize and determine the quality/purity of the crystals of BBP. Spectra for each crystal type were normalized to a certain peak (the exact position of the peak is indicated by arrows on the graphs and in the figure legends). For the Raman spectrum, the C–H stretching vibrations were observed at 1300–1000 cm^{-1}, showing a strong Raman intensity. The C–H out-of-plane deformations were observed at 703, 716, 738, 776, 813, 836, 871, 898, and 990 cm^{-1}. Moreover, peaks at 1297, 1327, 1421, and 1437 cm^{-1} crystal were observed and assigned to C–C stretching vibrations. A sharp band at 1599 cm^{-1} was also observed and assigned to ethylenic bridge vibrations. The C=O

vibrations were also observed as a weak Raman band at 1661 cm^{-1}. The C=O stretching vibration is further influenced by the intermolecular hydrogen bonding between the C=O group and phenyl ring, which may explain the weak Raman band observed. A Raman peak at 1070 cm^{-1} was used to normalize the spectrum. The characteristic curve and peaks observed in the TGA and DTG, respectively, are shown in Figure 6.
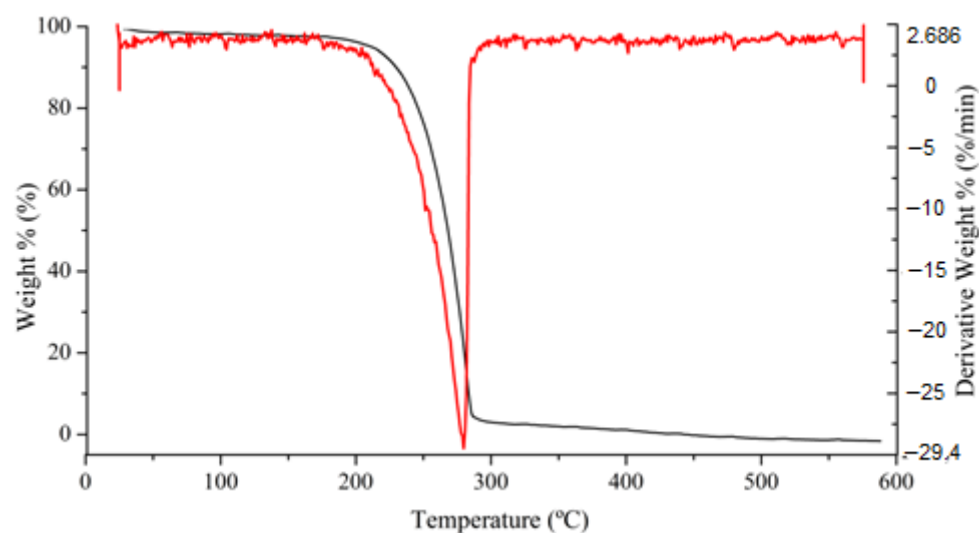
Figure 6. TGA and DTG of BBP.

Through the TGA curve, the decomposition of the BBP compound was observed as a well-defined event, represented by a single DTG peak. The DTG allowed us to see the temperatures corresponding to the beginning and end of the thermal event. The compound maintained its mass at temperatures close to 210 °C; then, after this point, one interval of great mass loss occurred until 300 °C, reaching almost 0% of the weight. Figure 7 displays the DSC traces and indicates a sharp exothermic peak at 109.8 °C for the heating of the chalcone crystal. The DSC thermogram indicates direct melting of the crystal phase to the isotropic liquid phase since the thermogram showed a single endotherm during the heating cycles. The enthalpy change (ΔH) was 31.71 kJ.mol^{-1}.
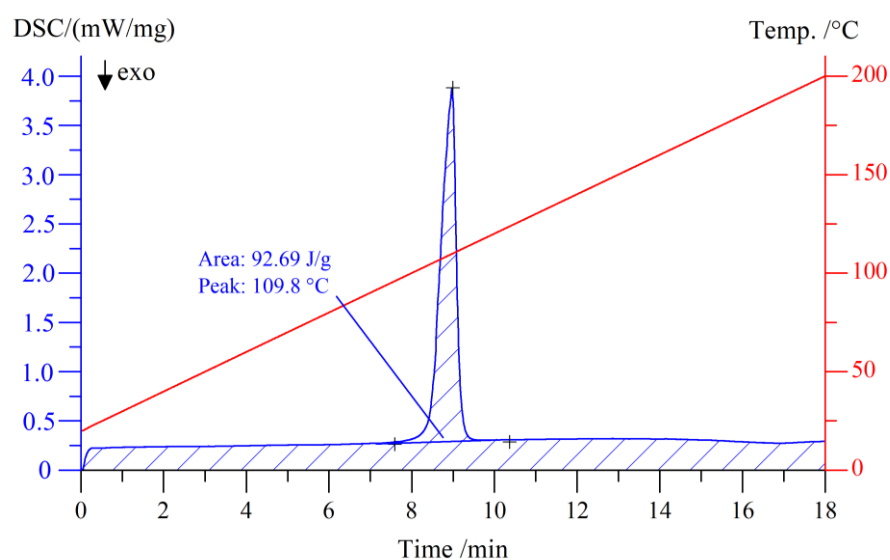
Figure 7. DSC measurement of BBP.

The UV-Vis absorption spectrum of BBP, Figure 8, clearly shows an absorption band at 336 nm, which can be attributed to the functional group $-C=C-CO$ and phenyl ring chromophore and shows a similarity with the chalcone-type molecules.
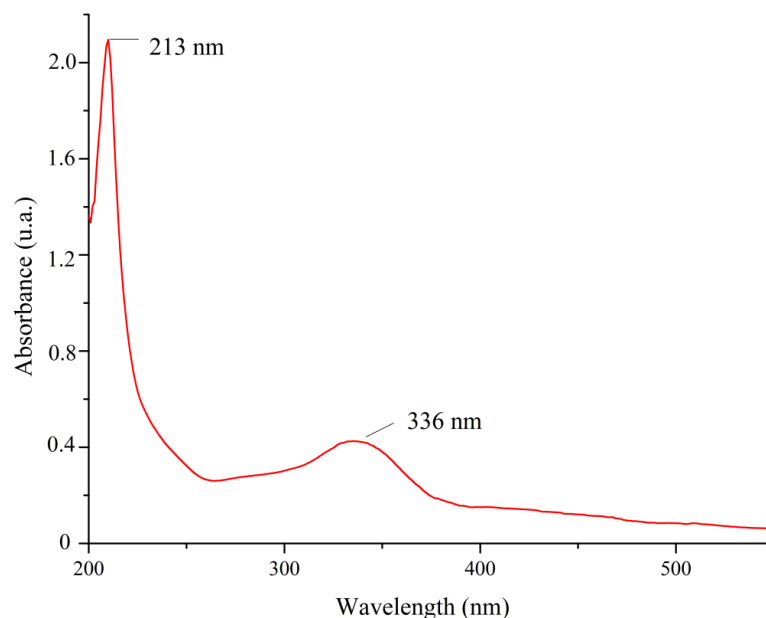
Figure 8. UV-vis spectrum of BBP in DMSO.

BBP shows a butyl group and a bromine atom ortho-bonded to aromatic rings A and B, respectively. It crystallizes into the Pbca space group with a single molecule in the asymmetric unit. The ortep representation, Figure 9, shows atomic ellipsoids with similar size and absence of disorder problem [39]. Comprehensive statistical analyses by Mogul software [44] confirmed the absence of any unusual bond distances, bond angles, and torsions on observed conformation. The main crystallographic refinement data are presented in Table 2.

Figure 9. Ortep diagram showing BBP molecule in the asymmetric unit drawing with 50% probability ellipsoid.

Table 2. Crystallographic parameters for BBP.

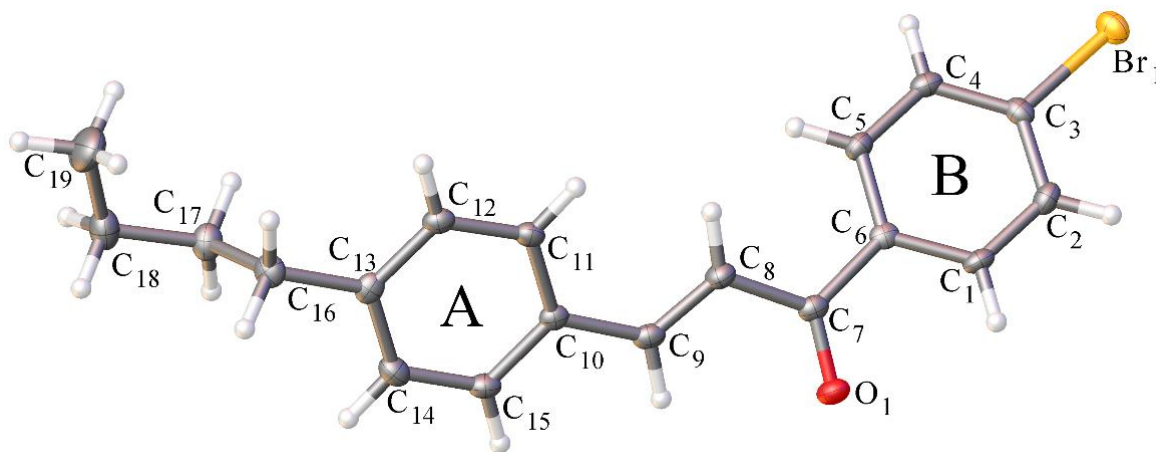| Crystal Data	
Chemical formula	$C_{19}H_{19}BrO$
Mr	343.25
Crystal system, space group	Orthorhombic, Pbca
Temperature (K)	120
a, b, c (Å)	11.3065 (12), 8.1831 (9), 33.892 (4)
V (Å3)	3135.8 (6)
Z	8
Radiation type	Mo Kα
μ (mm^{-1})	2.62
Crystal size (mm)	0.23 × 0.20 × 0.04
Data Collection	
Diffractometer	Bruker APEX-II CCD
Absorption correction	Multi-scan SADABS2016/2 (Bruker,2016/2) was used for absorption correction. wR2(int) was 0.0455 before and 0.0414 after correction. The Ratio of minimum to maximum transmission is 0.7126. The $\lambda/2$ correction factor is not present.
Tmin, Tmax	0.662, 0.929
No. of measured, independent and observed [I > 2σ(I)] reflections	42,969, 3878, 2966
Rint	0.062
(sin θ/λ)max (Å^{-1})	0.666
Refinement	
R [F2 > 2σ(F2)], wR(F2), S	0.032, 0.068, 1.03
No. of reflections	3878
No. of parameters	191
H-atom treatment	H-atom parameters constrained
$\Delta\rho$max, $\Delta\rho$min (e Å^{-3})	0.39, −0.39

Computer programs:Olex2.solve 1.3 [45] SHELXL 2018/3 [46], Olex2 1.3 [27].

Molecular planarity is an important parameter; the higher the number of donor–receptor interactions in a molecule, the better the electron transfer and nonlinearity. The planarity in the chalcones is related to donor–acceptor interactions across the main chain of chalcones, to π-conjugation throughout charge transfer [47,48]. The angle between the aromatic rings from BBP is 47.05° (Figure 10), being non-planar, decreasing the crystal packing energy and melting point, thus improving the aqueous solubility. In a search on CCDC version 5.41 (November 2019) the (E)-1-(4-bromophenyl)-3-phenylprop-2-en-1-one (BRCHAL) [49] was found, which has the chalcone moiety without the butyl group. It has two independent molecules in asymmetric unity with similar planarity (angles between their aromatic rings are 49.70° and 49.98° (Figure 11)); this structure was tested before with *Ae. aegypti*, and the results are presented in Table 3.
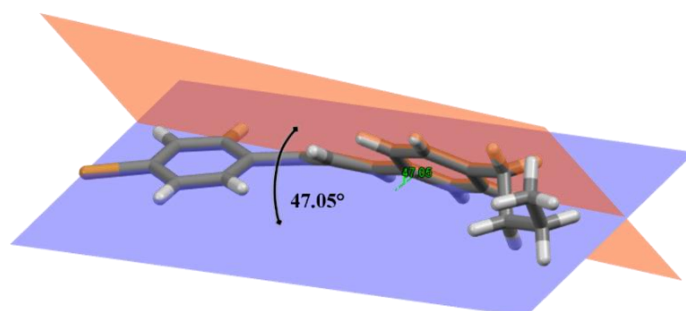
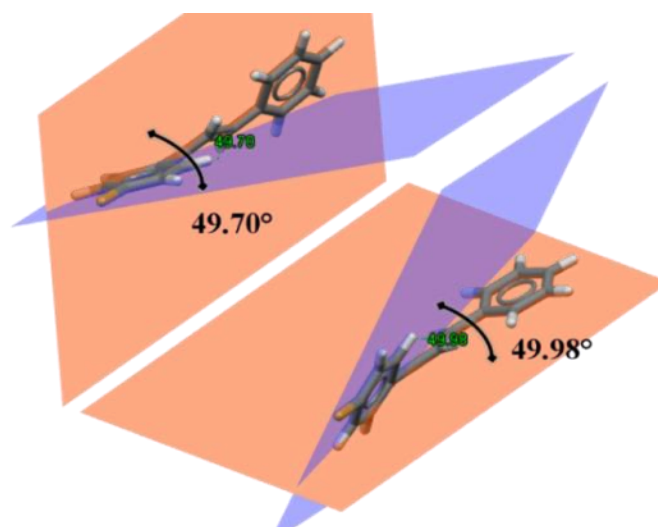**Figure 10.** Illustration of the angles between rings for BBP.

Figure 11. Illustration of the angles between rings for BRCHAL.

Table 3. Larvicidal activity of BBP on *A. aegypti* larvae (L3) after 48 h.

LC$_{25}$-48 h (mg·L^{-1}) *	LC$_{50}$-48 h (mg·L^{-1}) *	LC$_{75}$-48 h (mg·L^{-1}) *
37.7	46.0	54.2
(36.6–38.9)	(45.0–46.9)	(52.9–55.7)

* LC50, lethal concentration 50% mortality; LC25, lethal concentration 25% mortality; LC75, lethal concentration 75% mortality. Lethal concentrations in 48 h were calculated by non-linear regression of the respective dose–response curve, with a confidence interval of 95%. Values in parentheses represent lower and upper confidence limits of the interval.

The supramolecular arrangement of BPP is stabilized by C–H···O and the C–H···π. interactions, with donor–acceptor distances being shorter than the sum of the van der Waals radii (2.7 Å for O and H) [50]. The BPP crystal packing molecules in a layer along the a-axis are presented in Figure 8 and were responsible for joining the crystal by the C5–H5···O1 interaction (d/Å, θ/°: 2.67 Å, 148°), symmetry code, (i) x − 1/2, −y + 1/2, −z + 1, and was also stabilized by edge-to-face C12–H12···π interaction involving aromatic ring B, shown in Figure 12 [29]. This was confirmed by the shape index (I) that provides information regarding π···π and C–H···π, and dnorm surface(II), with C–H···O observed by the concave red region over aromatic ring B. Such interactions also explain the observed conformation of the molecular structure at BBP [25,27].

HS indicates the partition of crystal electron density into molecular fragments from the three-dimensional space occupied by a molecule, representing the regions of space in which molecules are in contact with each other [33]. Both donor and acceptor regions are considered by the dnorm surface, which is based on the normalized function of di (distance to the nearest nucleus internal to the surface) and de (distance from the point to the nearest nucleus external to the surface) [51]. The combination of di and de on a two-dimensional plot (fingerprint) in Figure 13 indicates the nature of intermolecular interaction [51]. The major interaction lies in H–H (50.04%) and C–H (21.6%), while the halogen Br gives (12.4%) of interaction with H, and C–H (21.6%). The H–H contacts are the closest contacts for HS [52].
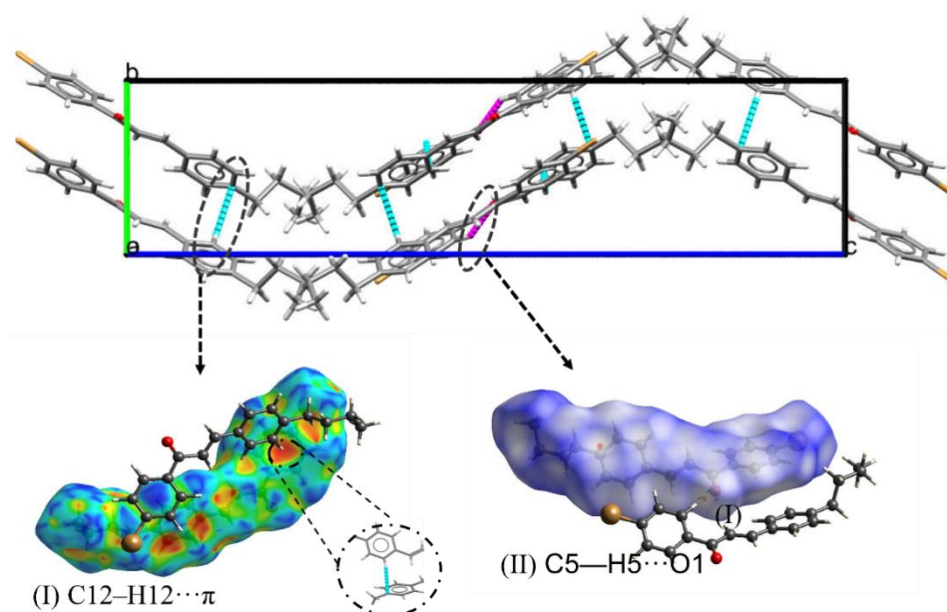
Figure 12. Present the packing stabilized by C–H···O and the C–H···π. Interactions that are confirmed by Hirshfeld surface shape index (**I**) showing the edge-to-face C–H···π interactions and the Hirshfeld surface dnorm map (**II**) showing C–H···O interactions for BBP.
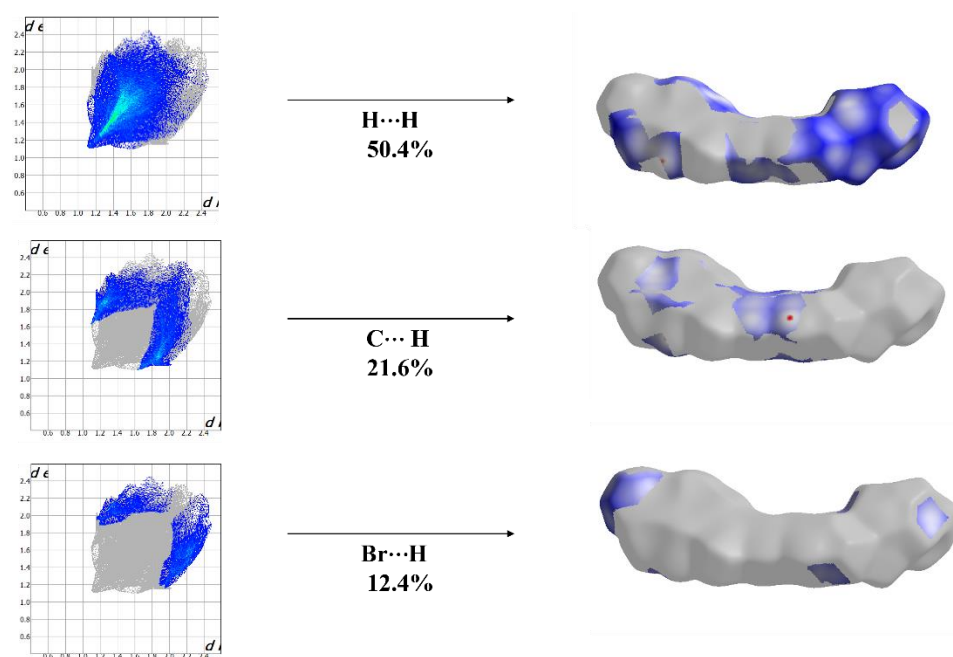
Figure 13. Hirshfeld surface diagram and two-dimensional fingerprint plots of the nearest internal distance (di) versus the nearest external distance (de) for major interactions in BBP.

The MEP map can be visualized reflecting the boundaries of the molecule, and it is useful to identify sites such as hydrogen bonds and regions where electrophilic and also nucleophilic attacks occur. This information can be used by electrostatic forces acting over long distances, exploring drug–receptor and enzyme–substrate interactions [53]. The molecular electrostatic potential V(r) at a point r is defined as Equation (1):

$$V(r) = \sum_i \frac{Z_i}{|R_i - r|} \int \left(\frac{\rho(r')}{|r' - r|} \right) dr' \qquad (2)$$

where Z_i is the charge at nucleus I located at R, and $\rho(r')$ is the molecular electron density at a point r' near the molecule [54]. Figure 14 shows the calculated MEP of BBP, showing regions that are well distinguished. Regions with negative electrostatic potential, i.e., C=O groups, are shown in red; regions with positive electrostatic potential are shown in blue, which means the region around the hydrogen atoms of the α,β-unsaturated ketone. This site tends to attract chemical species that are rich in electrons, while species poor in electrons will be attracted to the C=O region [37,40].
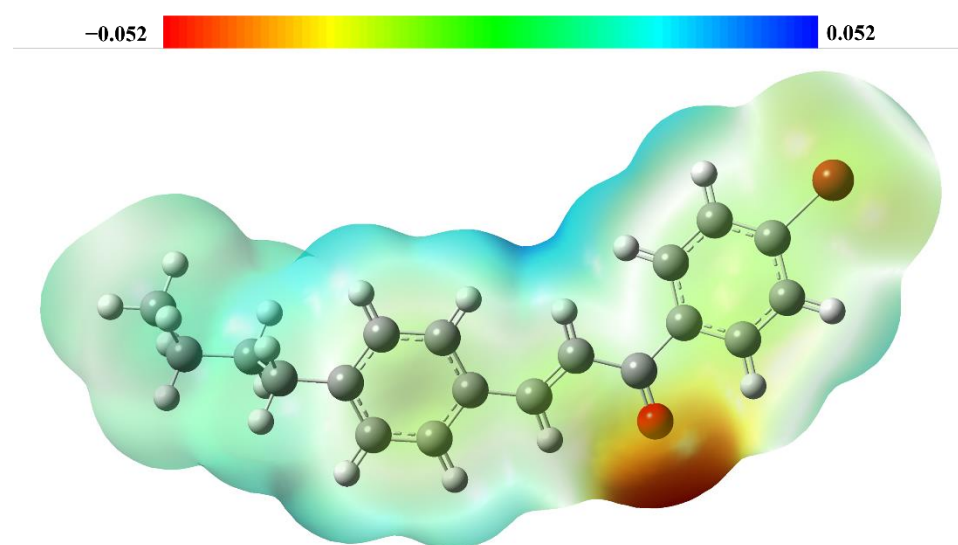

Figure 14. Molecular electrostatic potential map of BBP. The red region is rich in electrons, and the blue is electron depleted.

The frontier molecular orbitals (FMO) also play an important role in understanding chemical reaction mechanisms [42]. The LUMO and HOMO of other reactants interact with each other during the chemical process [53]. They are as follows: ELUMO = −2.57eV; EHOMO = −6.54eV. Their representations are presented in Figure 15.
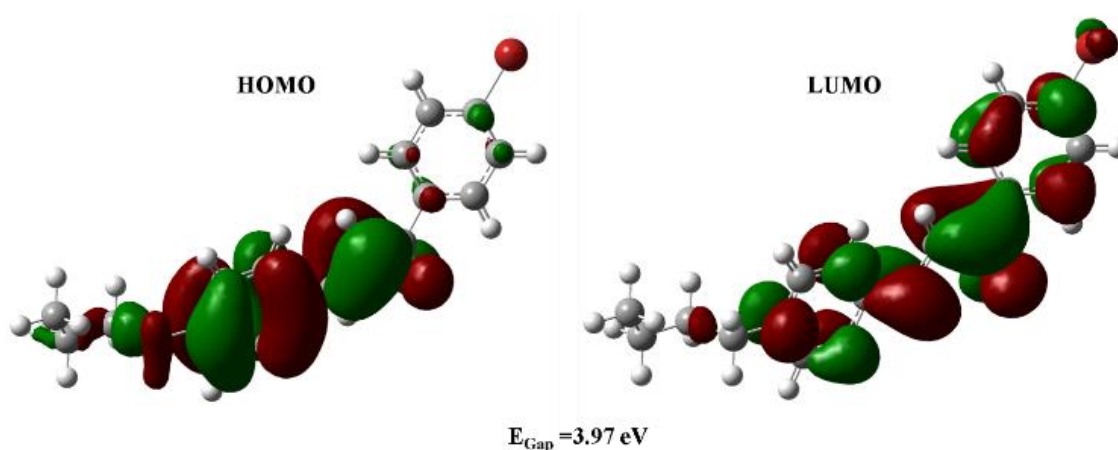
Figure 15. Graphical representation of the LUMO and HOMO and the calculated energy gap for BBP.

The energy gap between HOMO and LUMO is an important index for the stability of molecules, and a small gap automatically means small excitation energies for the manifold of excited states. Therefore, soft molecules, with a small gap, are more polarizable than hard molecules [55]. The energy values for these properties are: EGAP = 3.97 eV, hardness η = 1.78 eV, and softness σ = 0.56 eV. Comparing EGAP from BBP with other chalcone publications, ((E)-3-(4-ethoxyphenyl)-1-(4-methoxyphenyl)prop-2-en-1-one) has

EGAP = 6.4007 eV, and ((E)-1-(4-methoxyphenyl)-3-(3,4,5-trimethoxyphenyl) prop-2-en-1-one) EGAP = 6.2611 eV [56] as well as (E)-1-(2-aminophenyl)-3-(4-nitrophenyl)prop-2-en-1-one, with EGAP= 4.70 eV [57], but BBP presents a smaller EGAP value of 3.97 eV, so it is more reactive than these other chalcones.

3.3. Larvicidal Activity

According to The World Health Organization, larvicidal compounds should be active at concentrations value below 100 mg·L^{-1} [18,20,21]. Table 3 presents the larvicidal activity (LC25, LC50, and LC75) of BBP after 48 h. According to these results, BBP was effective against third-instar larvae (L3) of *A. aegypti*, showing LC50-48h = 46 mg·L^{-1}.

Recent studies have identified chalcone derivatives as anti-juvenile compounds (antagonists of the juvenile insect hormone) [19]. These natural product derivatives are important interferences in the physiological processes of insects, such as interference in ecdysis, metamorphosis, and reproduction, among others [19]. In addition, our results showed that, as well as lethality among larvae of *Ae. aegypti*, there was abnormal larval development (inhibition of ecdysis) when larvae were exposed to BBP concentrations below 20 mg.L^{-1}. Although there is no lethality at these concentrations, the larvae exposed to BBP for 48 h showed a gradual reduction in their mobility and lethargy compared to the control. Figure 16 shows larval mortality (%) as a function of BBP concentration.
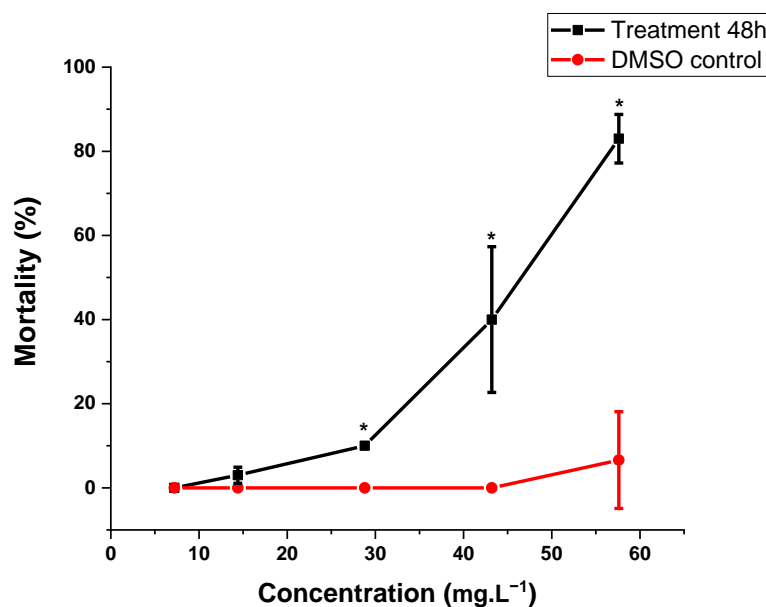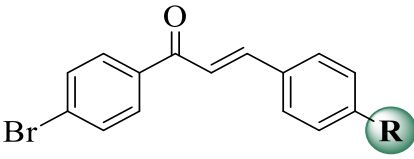
Figure 16. *Ae. aegypti* larvae mortality (%) as a function of BBP concentration (mg·L^{-1}). The symbol (*) indicates statistical significance with the DMSO group (ANOVA/Tukey; $p \leq 0.05$).

A mortality rate depends on the concentration of BBP used was observed, presenting a rate up to 80% at 57.6 mg L^{-1}, in 48 h (Figure 15). In comparison to the literature, the bromochalcone derivative (BBP) showed greater larvicidal activity than other bromochalcone derivatives evaluated by Kalirajan et al. (2015) on Culex sp. and Anopheles sp. [58]. Eight of these molecules showed LC50-24 h values greater than 50 mg·L^{-1}. Table 4 presents the structure–activity relationship of bromochalcone derivatives concerning *Ae. aegypti* larvae mortality (%).

Table 4. Structure–activity relationship of bromochalcone derivatives concerning *A. aegypti* larvae mortality (%).

Entry	R	Concentration (mg L^{-1})	Mortality (%)	Ref
1	H	100	70	[18]
2	NO$_2$	100	0	[18]
3	OMe	100	0	[18]
4	(CH$_2$)$_3$CH$_3$	54.2	75	This work

From the analysis of Table 4, there is a significant relationship between the molecular structure and the larvicidal activity of bromochalcone derivatives. Our results compared to the literature demonstrated that the presence of withdrawing groups e.g., (R = NO$_2$) and donating groups e.g., (R = OMe) decreased the larvicidal efficiency when compared to the unsubstituted chalcone (R = H). Additionally, that study revealed that the insertion of the butyl group at position 4 (R = (CH$_2$)$_3$CH$_3$) significantly increased the larvicidal activity of bromochalcone derivatives. This increase in the larvicidal activity of BBP may be related to the increase in its lipophilicity and interaction with biological membranes. The obtained results are promising, and bromochalcone derivatives may be a potential arsenal against *Ae. aegypti* larvae.

4. Conclusions

A bromochalcone derivative (BBP) was obtained in excellent yield and fully characterized by ^{1}H- and ^{13}C-NMR, IR, FT-Raman, MS, UV-Vis, TGA, and DSC. Moreover, according to the literature and our study, the substitution pattern of chalcone derivative influenced its larvicidal activity. In this regard, BBP (a bromo chalcone derivative), which presents a butyl group at position 4 (R = (CH$_2$)$_3$CH$_3$, significantly showed promising larvicidal activity (mortality up to 80% at 57.6 mg·L^{-1}) against *Ae. aegypti* larvae. BBP showed a non-planar molecular conformation with 2.9° of difference to BRCHAL(R=H) that presents 5% less mortality than BBP against *Ae. aegypti* larvae at 100 mg·L^{-1}, this difference between the planarity indicated a small improvement in the solubility in BBP compared with BRCHAL. The solid-state of BBP was stabilized by intermolecular interactions C–H···O and C–H···π, with theoretical calculations indicating electrophilic sites near oxygen atoms and depleted electrons around the hydrogen of the α,β-unsaturated ketone. The bandgap was 3.79, which is more polarizable than similar reported structures. Overall, we presented the synthesis, structural characterization, computational analysis, and full spectroscopy/thermal characterization of the BBP as well as its larvicidal activity against *Ae. aegypti* larvae.

Author Contributions: Conceptualization, P.P.F., L.D.D. and H.B.N.; methodology, J.E.Q., P.R.S.W., P.P.F. and W.F.V.; formal analysis P.P.F. and W.F.V.; investigation, P.P.F., W.F.V., L.M.d.S. and L.D.D.; resources, J.E.Q., I.I. and G.L.B.d.A.; data curation, P.P.F. and J.E.Q.; writing—original draft preparation, P.P.F., W.F.V., L.M.d.S., L.D.D. and J.M.F.C.; writing—review and editing, P.P.F., L.D.D. and P.R.S.W.; visualization, P.P.F. and L.D.D.; supervision H.B.N., G.L.B.d.A. and A.G.O.; funding acquisition, P.R.S.W. and H.B.N. All authors have read and agreed to the published version of the manuscript.

Institutional Review Board Statement: Not applicable.

Informed Consent Statement: Informed consent was obtained from all subjects involved in the study.

Data Availability Statement: Not applicable.

Conflicts of Interest: The authors declare no conflict of interest.

References

1. Cox, C.D.; Breslin, M.J.; Mariano, B.J. Two-Step Synthesis of β-Alkyl Chalcones and Their Use in the Synthesis of 3,5-Diaryl-5-Alkyl-4,5-Dihydropyrazoles. *Tetrahedron Lett.* **2004**, *45*, 1489–1493. [CrossRef]
2. Xu, M.; Wu, P.; Shen, F.; Ji, J.; Rakesh, K.P. Chalcone Derivatives and Their Antibacterial Activities: Current Development. *Bioorganic Chem.* **2019**, *91*, 103133. [CrossRef] [PubMed]
3. Ngaini, Z.; Haris Fadzillah, S.M.; Hussain, H. Synthesis and Antimicrobial Studies of Hydroxylated Chalcone Derivatives with Variable Chain Length. *Nat. Prod. Res.* **2012**, *26*, 892–902. [CrossRef] [PubMed]
4. Stepanić, V.; Matijašić, M.; Horvat, T.; Verbanac, D.; Chlupáčová, M.K.; Saso, L.; Žarković, N. Antioxidant Activities of Alkyl Substituted Pyrazine Derivatives of Chalcones—In Vitro and in Silico Study. *Antioxidants* **2019**, *8*, 90. [CrossRef] [PubMed]
5. Da Silva, P.T.; da Cunha Xavier, J.; Freitas, T.S.; Oliveira, M.M.; Coutinho, H.D.M.; Leal, A.L.A.B.; Barreto, H.M.; Bandeira, P.N.; Nogueira, C.E.S.; Sena, D.M.; et al. Synthesis, Spectroscopic Characterization and Antibacterial Evaluation by Chalcones Derived of Acetophenone Isolated from Croton Anisodontus Müll.Arg. *J. Mol. Struct.* **2021**, *1226*, 129403. [CrossRef]
6. Yadav, V.R.; Prasad, S.; Sung, B.; Aggarwal, B.B. The Role of Chalcones in Suppression of NF-KB-Mediated Inflammation and Cancer. *Int. Immunopharmacol.* **2011**, *11*, 295–309. [CrossRef]
7. Wang, G.; Liu, W.; Gong, Z.; Huang, Y.; Li, Y.; Peng, Z. Synthesis, Biological Evaluation, and Molecular Modelling of New Naphthalene-Chalcone Derivatives as Potential Anticancer Agents on MCF-7 Breast Cancer Cells by Targeting Tubulin Colchicine Binding Site. *J. Enzym. Inhib. Med. Chem.* **2020**, *35*, 139–144. [CrossRef]
8. Bonakdar, A.P.S.; Vafaei, F.; Farokhpour, M.; Esfahani, M.H.N.; Massah, A.R. Synthesis and Anticancer Activity Assay of Novel Chalcone-Sulfonamide Derivatives. *Iran. J. Pharm. Res.* **2017**, *16*, 565–568. [CrossRef]
9. Mellado, M.; Espinoza, L.; Madrid, A.; Mella, J.; Chávez-Weisser, E.; Diaz, K.; Cuellar, M. Design, Synthesis, Antifungal Activity, and Structure–Activity Relationship Studies of Chalcones and Hybrid Dihydrochromane–Chalcones. *Mol. Divers.* **2019**, *24*, 603–615. [CrossRef]
10. Zheng, Y.; Wang, X.; Gao, S.; Ma, M.; Ren, G.; Liu, H.; Chen, X. Synthesis and Antifungal Activity of Chalcone Derivatives. *Nat. Prod. Res.* **2015**, *29*, 1804–1810. [CrossRef]
11. Lahsasni, S.A.; Al Korbi, F.H.; Aljaber, N.A.A. Synthesis, Characterization and Evaluation of Antioxidant Activities of Some Novel Chalcones Analogues. *Chem. Cent. J.* **2014**, *8*, 32. [CrossRef]
12. Díaz-Carrillo, J.T.; Díaz-Camacho, S.P.; Delgado-Vargas, F.; Rivero, I.A.; López-Angulo, G.; Sarmiento-Sánchez, J.I.; Montes-Avila, J. Synthesis of Leading Chalcones with High Antiparasitic, against Hymenolepis Nana, and Antioxidant Activities. *Braz. J. Pharm. Sci.* **2018**, *54*, 1–13. [CrossRef]
13. AID 371504—Antiamnesic Activity against Entamoeba Histolytica HMI:IMSS after 72 Hrs by Microdilution Method—PubChem. Available online: https://pubchem.ncbi.nlm.nih.gov/bioassay/371504#sid=103590847 (accessed on 29 October 2020).
14. Chhabra, M.; Mittal, V.; Bhattacharya, D.; Rana, U.V.S.; Lal, S. Chikungunya Fever: A Re-Emerging Viral Infection. *Indian J. Med. Microbiol.* **2008**, *26*, 5–12. [CrossRef]
15. WHO. Dengue and Severe Dengue. Available online: https://www.who.int/news-room/fact-sheets/detail/dengue-and-severe-dengue (accessed on 18 February 2021).
16. Ghosh, A.; Dar, L. Dengue Vaccines: Challenges, Development, Current Status and Prospects. *Indian J. Med. Microbiol.* **2015**, *33*, 3–15. [CrossRef] [PubMed]
17. Barbosa, P.B.B.M.; de Oliveira, J.M.; Chagas, J.M.; Rabelo, L.M.A.; de Medeiros, G.F.; Giodani, R.B.; da Silva, E.A.; Uchôa, A.F.; de Fátima de Freire Melo Ximenes, M. Evaluation of Seed Extracts from Plants Found in the Caatinga Biome for the Control of Aedes Aegypti. *Parasitol. Res.* **2014**, *113*, 3565–3580. [CrossRef] [PubMed]
18. Targanski, S.K.; Sousa, J.R.; de Pádua, G.M.S.; de Sousa, J.M.; Vieira, L.C.C.; Soares, M.A. Larvicidal Activity of Substituted Chalcones against Aedes Aegypti (Diptera: Culicidae) and Non-Target Organisms. *Pest Manag. Sci.* **2021**, *77*, 325–334. [CrossRef]

19. Lee, S.H.; Oh, H.W.; Fang, Y.; An, S.B.; Park, D.S.; Song, H.H.; Oh, S.R.; Kim, S.Y.; Kim, S.; Kim, N.; et al. Identification of Plant Compounds That Disrupt the Insect Juvenile Hormone Receptor Complex. *Proc. Natl. Acad. Sci. USA* **2015**, *112*, 1733–1738. [CrossRef]

20. Cheng, S.S.; Chang, H.T.; Chang, S.T.; Tsai, K.H.; Chen, W.J. Bioactivity of Selected Plant Essential Oils against the Yellow Fever Mosquito Aedes Aegypti Larvae. *Bioresour. Technol.* **2003**, *89*, 99–102. [CrossRef]

21. WHO and Special Programme for research and Training in Tropical Diseases. *Dengue Guidelines for Diagnosis, Treatment, Prevention and Control*; World Health Organization: Geneva, Switzerland, 2009; pp. 1–144. ISBN 9789241547871.

22. Ternavisk, R.R.; Camargo, A.J.; Machado, F.B.C.; Rocco, J.A.F.F.; Aquino, G.L.B.; Silva, V.H.C.; Napolitano, H.B. Synthesis, Characterization, and Computational Study of a New Dimethoxy-Chalcone. *J. Mol. Modeling* **2014**, *20*, 2526. [CrossRef]

23. Pence, I.; Mahadevan-jansen, A. Clinical instrumentation and applications of Raman spectroscopy. *Chem. Soc. Rev.* **2016**, *45*, 1958–1979. [CrossRef]

24. Mitsutake, H.; Poppi, R.J.; Breitkreitz, M.C. Raman Raman Imaging Imaging Spectroscopy: Spectroscopy: History, History, Fundamentals Fundamentals and Current and Current Scenario Scenario of the Oftechnique the Technique. *J. Braz. Chem. Soc.* **2019**, *30*, 2243–2258. [CrossRef]

25. Bolton, E.E.; Wang, Y.; Thiessen, P.A.; Bryant, S.H. *Chapter 12 PubChem: Integrated Platform of Small Molecules and Biological Activities*; Elsevier B.V.: Amsterdam, The Netherlands, 2008; Volume 4, ISBN 9780444532503.

26. Sheldrick, G.M. A Short History of SHELX. *Acta Crystallogr. Sect. A Found. Crystallogr.* **2008**, *64*, 112–122. [CrossRef]

27. Dolomanov, O.V.; Bourhis, L.J.; Gildea, R.J.; Howard, J.A.K.; Puschmann, H. OLEX2: A Complete Structure Solution, Refinement and Analysis Program. *J. Appl. Crystallogr.* **2009**, *42*, 339–341. [CrossRef]

28. Sheldrick, G.M. Crystal Structure Refinement with SHELXL. *Acta Crystallogr. Sect. C Struct. Chem.* **2015**, *71*, 3–8. [CrossRef] [PubMed]

29. Spek, A.L. Structure Validation in Chemical Crystallography. *Acta Crystallogr. Sect. D Biol. Crystallogr.* **2009**, *65*, 148–155. [CrossRef]

30. Kanagasabai, S.; Gugan, K.; Reddy, M.B.; Anandhan, R.; Kumar, S.M.; Usharani, S. Crystal Structure and Hirshfeld Surface Analysis of 2,2′-Bi-(3-Phenyl-2H-1,4-Benzothiazine). *Chem. Data Collect.* **2019**, *20*, 1564–1567. [CrossRef]

31. Abad, N.; Ramli, Y.; Hökelek, T.; Sebbar, N.K.; Mague, J.T.; Essassi, E.M. Crystal Structure and Hirshfeld Surface Analysis of Ethyl 2-{4-[(3-Methyl-2-Oxo-1,2-Dihydroquinoxalin- 1-Yl)Methyl]-1H-1,2,3-Triazol-1-Yl}acetate. *Acta Crystallogr. Sect. E Crystallogr. Commun.* **2018**, *74*, 1648–1652. [CrossRef]

32. McKinnon, J.J.; Jayatilaka, D.; Spackman, M.A. Towards Quantitative Analysis of Intermolecular Interactions with Hirshfeld Surfaces. *Chem. Commun.* **2007**, 3814–3816. [CrossRef]

33. Spackman, M.A.; Jayatilaka, D. Hirshfeld Surface Analysis. *CrystEngComm* **2009**, *11*, 19–32. [CrossRef]

34. Spackman, P.R.; Turner, M.J.; McKinnon, J.J.; Wolff, S.K.; Grimwood, D.J.; Jayatilaka, D.; Spackman, M.A. CrystalExplorer: A Program for Hirshfeld Surface Analysis, Visualization and Quantitative Analysis of Molecular Crystals. *J. Appl. Crystallogr.* **2021**, *54*, 1006–1011. [CrossRef]

35. Frisch, M.J.; Trucks, G.W.; Schlegel, H.B.; Scuseria, G.E.; Robb, M.A.; Cheeseman, J.R.; Scalmani, G.; Barone, V.; Mennucci, B.; Petersson, G.A.; et al. Gaussian 09 2009. Available online: https://gaussian.com/gaussian16/ (accessed on 28 February 2022).

36. Custodio, J.M.F.; Michelini, L.J.; De Castro, M.R.C.; Vaz, W.F.; Neves, B.J.; Cravo, P.V.L.; Barreto, F.S.; Filho, M.O.M.; Perez, C.N.; Napolitano, H.B. Structural Insights into a Novel Anticancer Sulfonamide Chalcone. *New J. Chem.* **2018**, *42*, 3426–3434. [CrossRef]

37. Sallum, L.O.; Siqueira, V.L.; Custodio, J.M.F.; Borges, N.M.; Lima, A.P.; Abreu, D.C.; De Lacerda, E.P.S.; Lima, R.S.; De Oliveira, A.M.; Camargo, A.J.; et al. Molecular Modeling of Cytotoxic Activity of a New Terpenoid-like Bischalcone. *New J. Chem.* **2019**, *43*, 18451–18460. [CrossRef]

38. Haroon, M.; Khalid, M.; Akhtar, T.; Tahir, M.N.; Khan, M.U.; Saleem, M.; Jawaria, R. Synthesis, Spectroscopic, SC-XRD Characterizations and DFT Based Studies of Ethyl2-(Substituted-(2-Benzylidenehydrazinyl))Thiazole-4-Carboxylate Derivatives. *J. Mol. Struct.* **2019**, *1187*, 164–171. [CrossRef]

39. Moreira, C.A.; Custódio, J.M.F.; Vaz, W.F.; D'Oliveira, G.D.C.; Noda Perez, C.; Napolitano, H.B. A Comprehensive Study on Crystal Structure of a Novel Sulfonamide-Dihydroquinolinone through Experimental and Theoretical Approaches. *J. Mol. Modeling* **2019**, *25*, 205. [CrossRef]

40. Medina, D.; Menezes, A.C.S.; Sousa, J.E.F.; Oliveira, S.S. Structural and Theoretical Investigation of Anhydrous 3, 4, 5-Triacetoxybenzoic Acid. *PLoS ONE* **2016**, *11*, e0158029. [CrossRef]

41. Merrick, J.P.; Moran, D.; Radom, L. An Evaluation of Harmonic Vibrational Frequency Scale Factors. *J. Phys. Chem. A* **2007**, *111*, 11683–11700. [CrossRef]

42. Aguiar, A.S.N.; Queiroz, J.E.; Firmino, P.P.; Vaz, W.F.; Camargo, A.J.; de Aquino, G.L.B.; Napolitano, H.B.; Oliveira, S.S. Synthesis, Characterization, and Computational Study of a New Heteroaryl Chalcone. *J. Mol. Modeling* **2020**, *26*, 243. [CrossRef]

43. Millam, R.D.; Todd, A.; Keith John, M. GaussView Version 6. 2019. Available online: https://gaussian.com/gaussview6/ (accessed on 28 February 2022).

44. Cottrell, S.J.; Olsson, T.S.G.; Taylor, R.; Cole, J.C.; Liebeschuetz, J.W. Validating and Understanding Ring Conformations Using Small Molecule Crystallographic Data. *J. Chem. Inf. Modeling* **2012**, *52*, 956–962. [CrossRef]

45. Bourhis, L.J.; Dolomanov, O.V.; Gildea, R.J.; Howard, J.A.K.; Puschmann, H. The Anatomy of a Comprehensive Constrained, Restrained Refinement Program for the Modern Computing Environment—Olex2 Dissected. *Acta Crystallogr. Sect. A Found. Crystallogr.* **2015**, *71*, 59–75. [CrossRef]

46. Sheldrick, G.M. SHELXT—Integrated Space-Group and Crystal-Structure Determination. *Acta Crystallogr. Sect. A Found. Crystallogr.* **2015**, *71*, 3–8. [CrossRef]

47. Custodio, J.M.F.; Gotardo, F.; Vaz, W.F.; D'Oliveira, G.D.C.; de Almeida, L.R.; Fonseca, R.D.; Cocca, L.H.Z.; Perez, C.N.; Oliver, A.G.; de Boni, L.; et al. Benzenesulfonyl Incorporated Chalcones: Synthesis, Structural and Optical Properties. *J. Mol. Struct.* **2020**, *1208*, 127845. [CrossRef]

48. Rajesh Kumar, P.C.; Ravindrachary, V.; Janardhana, K.; Manjunath, H.R.; Karegouda, P.; Crasta, V.; Sridhar, M.A. Optical and Structural Properties of Chalcone NLO Single Crystals. *J. Mol. Struct.* **2011**, *1005*, 1–7. [CrossRef]

49. Rabinovich, D.; Schmidt, G.M.J.; Shaked, Z. Topochemistry. Part XXXIV. Crystal and Molecular Structure of P′-Bromochalcone. *J. Chem. Soc. Perkin Trans. 2* **1973**, *1*, 33–37. [CrossRef]

50. Johnston, R.C.; Cheong, P.H.Y. C-H···O Non-Classical Hydrogen Bonding in the Stereomechanics of Organic Transformations: Theory and Recognition. *Org. Biomol. Chem.* **2013**, *11*, 5057–5064. [CrossRef] [PubMed]

51. Vaz, W.F.; Custodio, J.M.F.; D'Oliveira, G.D.C.; Neves, B.J.; Junior, P.S.C.; Filho, J.T.M.; Andrade, C.H.; Perez, C.N.; Silveira-Lacerda, E.P.; Napolitano, H.B. Dihydroquinoline Derivative as a Potential Anticancer Agent: Synthesis, Crystal Structure, and Molecular Modeling Studies. *Mol. Divers.* **2021**, *25*, 55–66. [CrossRef]

52. Mkaouar, I.; Karâa, N.; Hamdi, B.; Zouari, R. Synthesis, Crystal Structure, Thermal Analysis, Vibrational Study Dielectric Behaviour and Hirshfeld Surface Analysis of $[C_6H_{10}(NH_3)_2)]_2$ $SnCl_6$ $(Cl)_2$. *J. Mol. Struct.* **2016**, *1115*, 161–170. [CrossRef]

53. Oliveira, S.S.; Santin, L.G.; Almeida, L.R.; Malaspina, L.A.; Lariucci, C.; Silva, J.F.; Fernandes, W.B.; Aquino, G.L.B.; Gargano, R.; Camargo, A.J.; et al. Synthesis, Characterization, and Computational Study of the Supramolecular Arrangement of a Novel Cinnamic Acid Derivative. *J. Mol. Modeling* **2017**, *23*, 35. [CrossRef]

54. Chidangil, S.; Shukla, M.K.; Mishra, P.C. A Molecular Electrostatic Potential Mapping Study of Some Fluoroquinolone Anti-Bacterial Agents. *J. Mol. Modeling* **1998**, *4*, 250–258. [CrossRef]

55. Vaz, W.F.; Custodio, J.M.F.; Silveira, R.G.; Castro, A.N.; Campos, C.E.M.; Anjos, M.M.; Oliveira, G.R.; Valverde, C.; Baseia, B.; Napolitano, H.B. Synthesis, Characterization, and Third-Order Nonlinear Optical Properties of a New Neolignane Analogue. *RSC Adv.* **2016**, *6*, 79215–79227. [CrossRef]

56. Custodio, J.; Faria, E.; Sallum, L.; Duarte, V.; Vaz, W.; de Aquino, G.; Carvalho Jr., P.; Napolitano, H. The Influence of Methoxy and Ethoxy Groups on Supramolecular Arrangement of Two Methoxy-Chalcones. *J. Braz. Chem. Soc.* **2017**, *28*, 2180–2191. [CrossRef]

57. Michelini, L.J.; Castro, M.R.C.; Custodio, J.M.F.; Naves, L.F.N.; Vaz, W.F.; Lobón, G.S.; Martins, F.T.; Perez, C.N.; Napolitano, H.B. A Novel Potential Anticancer Chalcone: Synthesis, Crystal Structure and Cytotoxic Assay. *J. Mol. Struct.* **2018**, *1168*, 309–315. [CrossRef]

58. Kalirajan, R.; Jubie, S.; Gowramma, B. Microwave Irradated Synthesis, Characterization and Evaluation for Their Antibacterial and Larvicidal Activities of Some Novel Chalcone and Isoxazole Substituted 9-Anilino Acridines. *Open J. Chem.* **2015**, *1*, 1–7. [CrossRef]